

## Article

# Developing Low-pH 3D Printing Concrete Using Solid Wastes

Xiao-Sheng Li \*, Long Li and Shuai Zou

Department of Civil and Environmental Engineering, The Hong Kong Polytechnic University, Hung Hom, Kowloon, Hong Kong, China

\* Correspondence: xiao-sheng.li@polyu.edu.hk

**Abstract:** Three-dimensional concrete printing technology provides the possibility to fabricate specific and eco-friendly concrete components for application on shorelines or in other areas, providing environmental protection. In this study, solid wastes in Hong Kong are employed for low-pH 3D printing concrete to further decrease the impact on the environment. The results indicate that WGP replacement in a classic low-pH recipe leads to lower yield stress and surface pH, as well as volume stability. The employment of slag improves workability and printability, but maintains the surface pH and drying shrinkage. The printing height is not merely determined by slump flow, and contributions from every binder on the surface pH are quantified based on simplified calculations. Reducing OPC and increasing SF in the classic low-pH recipe achieves the best printing performance and improved environmental friendliness.

**Keywords:** 3D concrete printing; low pH; low carbon; buildability

## 1. Introduction

When manufacturing the cement-based structural component to be applied under the sea or in contact with groundwater, its environmental impact on animals and plants has to be controlled, with restrictions on the pore solution of matrix. Low-pH cementitious materials are frequently employed for structure fabrication in flowing water environments. This material system employs a binding system with a pore solution pH below 11.0, after suitable employment of silica fume (SF) [1–3]. Generally, no more than 20% SF is suggested to be applied to the conventional concrete [4–8]. SF in high dosage (over 30%), required by low-pH concrete, significantly increases the viscosity and yield stress of the mixture, which is the fundamental elements for 3D concrete printing [1,9,10]. Therefore, achieving 3D concrete printing with a low-pH recipe possesses natural advantages.

Regarding the subversive manufacturing of concrete, 3D concrete printing technology has attracted significant attention ever since its invention [11–14]. It should be noted that mortar, rather than concrete, is the main choice of ink during 3D concrete printing, as mortar has a binder content that is much higher than that of concrete. Excessive binder tends to induce obvious volume instability. Therefore, shrinkage control should be provided, and reducing the cement content is a strategy that must be adopted to improve the volume stability [15–17]. Therefore, solid wastes are widely verified and applied in 3D concrete printing. This approach compensates for the possible performance decline induced by cement reduction and contributes to low-carbon strategy.

In a previous study, flash-calcined dredged sediment was applied into 3D concrete printing, resulting in an increase in the shape-retention ability [18]. Multiple industrial wastes have been employed in the printing system, with the ternary system with 20 wt.% fly ash, 15 wt.% silica fume, and 10 wt.% ground granulated blast furnace slag exhibiting the best printability and mechanical strength [8]. Replacement of 35 wt.% cement with fly ash is shown to achieve more suitable physical properties and printing behaviors, along with improved environmental friendliness [19]. Rice husk ash replacement is determined to improve the strength of fresh concrete, significantly modifying the rheology required for



**Citation:** Li, X.-S.; Li, L.; Zou, S. Developing Low-pH 3D Printing Concrete Using Solid Wastes. *Buildings* **2023**, *13*, 454. <https://doi.org/10.3390/buildings13020454>

Academic Editor: Elena Ferretti

Received: 28 December 2022

Revised: 30 January 2023

Accepted: 1 February 2023

Published: 7 February 2023



**Copyright:** © 2023 by the authors. Licensee MDPI, Basel, Switzerland. This article is an open access article distributed under the terms and conditions of the Creative Commons Attribution (CC BY) license (<https://creativecommons.org/licenses/by/4.0/>).

printing [20]. The use of 30 wt.% mining tailings induces reasonable mechanical strength and favorable buildability [21].

Waste glass is one of the main solid wastes in Hong Kong, generated from modern industry and inducing significant landfill problems during the past several decades. Attributed to its high stability, the waste glass cannot be digested by soil and could cause further incontinence to the environment. Thanks to the high alkaline setting in a cementitious environment, waste glass powder (WGP) gradually dissolves in the pore solution and generates hydration products (C-S-H gels) during later ages [22–25]. Researchers have studied the feasibility of incorporating WGP into 3D concrete printing. WGP is applied to replace river sand, revealing that a 100% substitution decreases plastic viscosity and dynamic yield stress [26], while a 50% volume replacement of crushed fine aggregate with WGP results in higher flexural and compressive strength after 28 days of standard curing [27]. The influence of the gradation of recycled glass on flexural strength and the microstructure of 3DCP is investigated, revealing that the replacement of natural sand with WGP decreases flexural strength and increases total porosity [28]. It has also been found that 25%, 50%, 75%, and 100% replacement of river sand with glass cullet leads to decreases in static yield stress, compressive strength, and interlayer bond strength, while the dynamic yield stress and plastic viscosity are improved [29]. However, previous research does not take advantage of possible low-pH properties during the incorporation of WGP into 3D printing.

Incinerated sewage sludge ash (ISSA) is the product generated from the calcination of sewage sludge obtained from the sewage treatment of industrial or municipal wastewater. The obvious porous structure induced by calcination significantly increases the water demand and long-term dry shrinkage [30–33]. Previous research indicates the potential of ISSA as the powder-bed 3D printed geopolymers [34]. Only limited investigations have been conducted related to the application of ISSA in 3D concrete printing. However, ISSA is believed to remarkably modify the yield stress and corresponding buildability of the mixture because of its high water absorption. Buildability is the parameter used to evaluate the capacity for shape maintenance after being extruded by the printer, and it can be determined by shear or compressive testing at an extremely early age. Therefore, employing ISSA should further contribute to a low pH and low carbon emission system.

In this study, WGP, slag, and ISSA are employed to further modify the classic low-pH recipe for 3D printed concrete. Workability, printability, and surface observation are applied to verify the feasibility of the proposed strategy in terms of 3D printing. Surface pH, volume stability, and mechanical property are evaluated correspondingly. Moreover, the relevance between workability and printability is discussed based on experimental results.

## 2. Materials and Methods

### 2.1. Materials

In this project, CEM 52.5 N cement (OPC), SF, WGP, slag, and ISSA were selected as binders and wastes. OPC was purchased from Green Island Cement (Holdings) Limited in Hong Kong. SF was purchased from Elkem Microsilica<sup>®</sup> 920 NA Concrete applications. The WGP was milled from post-consumer beverage bottles collected from a glass waste recycling facility in Hong Kong. Slag was obtained from mainland China. The ISSA used in this research was directly collected from the local sewage sludge incineration plant (T-park), and it had been classified as a non-hazardous material with low leaching risks.

Table 1 demonstrates the chemical composition and physical properties of the binder and wastes. The density of the binder and wastes are characterized with Lee's pycnometer. ISSA possesses a porous structure and lower density. Density can be applied to explain the unit weight results. Chemical compositions reveal the main chemical elements in the substances, which contain the information regarding mineral compositions, and can be applied to explain the obtained pH. Chemical compositions are analyzed with Rigaku Supermini200 X-ray Fluorescence. The specific surface area describes the particle size of

the powders and is used to explain the workability and mechanical properties. The specific surface area is obtained with the Malvern Mastersizer 3000 Particle Size Analyzer.

**Table 1.** Chemical composition and physical properties of the binder and wastes.

Material	OPC	SF	WGP	Slag	ISSA	
Chemical compositions (wt.%)	SiO <sub>2</sub>	18.7	95.9	69	31.5	37
	Al <sub>2</sub> O <sub>3</sub>	4.4	-	2.6	16.1	15.2
	CaO	68.1	0.1	10.5	40.2	6.9
	MgO	-	0.2	1.4	8	2.8
	SO <sub>3</sub>	5.2	3.2	0.1	2.3	3.7
	Fe <sub>2</sub> O <sub>3</sub>	2.7	0.1	1.4	0.3	14
	K <sub>2</sub> O	0.6	0.4	0.8	0.6	2.8
	Na <sub>2</sub> O	0.3	-	13.5	-	7.1
Density (g/cm <sup>3</sup> )	3.04	2.76	2.32	2.87	2.29	
Specific surface area (m <sup>2</sup> /kg)	761.1	5658	460.6	666.3	152.3	

Figure 1 demonstrates the gradation of river sand applied during 3D printing. The river sand is prepared by sieving out the particles larger than 1.7 mm. In this study, this strategy is used to ensure that the prepared mortar can be successfully extruded by a nozzle with a diameter of 10 mm. Figure 2 displays the particle size distribution of OPC and WGP, from which it can be seen that WGP possesses a lower particle size compared to OPC.

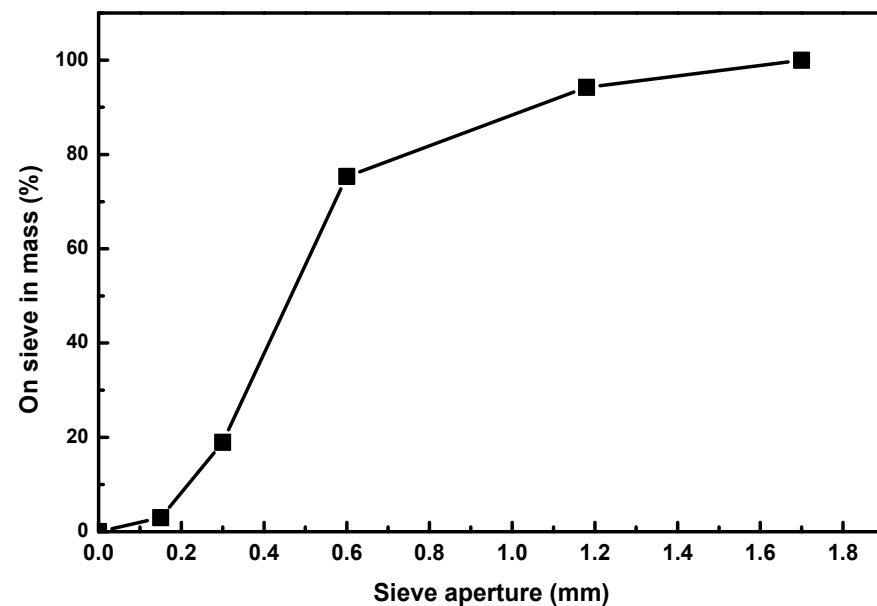


**Figure 1.** Gradation of river sand.

Polypropylene fiber (PP fiber), 6 mm in size, was purchased from an environmental additive supplier in mainland China. Superplasticizer (SP, powder in polycarboxylic acid form) and hydroxypropyl methyl cellulose ether (HPMC, powder) were obtained from Shanghai Chenqihuangong Limited in mainland China.

More importantly, the 3D concrete printing material of material A produced by local concrete enterprise in Hong Kong was studied comparatively. As far as we know, material A is composed of alkali activated binder, sand, retardant, and an expansive agent.

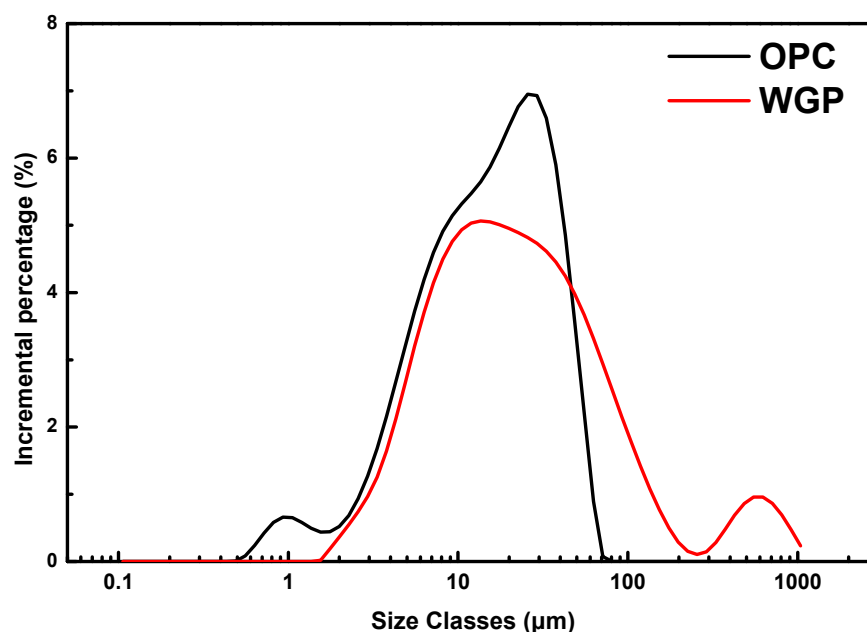


Figure 2. Particle size distribution of OPC and WGP.

## 2.2. Sample Preparation

Table 2 presents the mix proportion used in this study. The M-R group indicates the reference mix, the M-WGP group stands for the glass powder-modified mix, the M-GGBS group denotes the slag-modified mix, the M-ISSA group represents the ISSA-modified mix, and M-A designates the mix prepared with material A. Material A is purchased from a local concrete company in Hong Kong, and the mix proportions of the commercial product are confidential. In this study, M-A is applied to verify the printing performance of our materials. The M-R group is modified from a basic printable mix presented by Zou et al. [35–37]. This is because SF is considered to be the essential component for low-pH concrete [1,9,10]. The M-R group with 60% OPC and 40% SF is the classic low pH recipe, and it is widely used in different countries [38]. Furthermore, WGP, slag, and ISSA are employed to further improve the volume stability, mechanical properties, and printability. The principle for SP adjustment is to maintain the slump flow of 180 mm, which ensures suitable workability for printing, as determined by [39]. Adjustment of HPMC occurs when the mortar is too sticky to print. The design of mix proportions starts from the principle of prioritized printability and induces variation towards additives dosage, respectively. This strategy is adopted to thoroughly explore the printing possibility of the investigated materials and to avoid deficiency on discussions related to printing behaviors. Overall, it can be noticed that a lower SP is needed after the incorporation of WGP or GGBS, which is mainly related to the smaller particle size of WGP compared to OPC and SF. ISSA induces more sticky workability, and HPMC is reduced correspondingly.

Table 2. Mix proportion in this study (g).

ID <sup>a</sup>	OPC	SF	WGP	Slag	ISSA	Sand	Tap Water	PP Fiber	SP	HPMC
M-R	600	400	0	0	0	1000	350	5	4.4	1
M-WGP	400	200	400	0	0	1000	350	5	3.1	1
M-GGBS	200	400	0	400	0	1000	350	5	4.0	1
M-ISSA	500	300	0	0	200	1000	350	5	4.1	0.5

<sup>a</sup> The mix proportions of the commercial product are confidential.

The mixing procedures include two steps. Firstly, all materials except for water are mixed for 2 min (dry mixing). Then, water is incorporated gradually and the mixture is continuously stirred for 3 min (wet mixing). For standard curing, the specimens are demolded after one day and stored in saturated lime water at 20 °C. For steam curing, the specimens are demolded after one day and stored in a steam curing chamber at 65 °C.

### 2.3. Testing Methods

#### 2.3.1. Slump Flow

The slump flow of mortar is evaluated based on the methods in [40]. Firstly, the mortar is filled into the specific mold designed for mortar slump. Thereafter, two perpendicular diameters are recorded after jolting the flow table 25 times. The mini-slump cone and the flow table are shown in Figure 3. The adhesion of the sticky mortar to the molds can be efficiently prevented by prewetting the molds.



**Figure 3.** Mini-slump cone and flow table applied in this study.

#### 2.3.2. Buildability

Buildability is evaluated by shape-retention ability. Firstly, the cast-iron mold for the slump testing is filled with mortar. Then, after the removal of the mold, the mortar is left still and covered with a glass plate. Lastly, 1 kg weight is placed on the glass plate and the decreased height is recorded. This method is modified from the technique used in previous research [41].

#### 2.3.3. Rheology

This is evaluated with a RST CC rheometer produced by Brookfield. The vane used exhibits the sign of 40–20 MB. Figure 4 demonstrates the program applied in this study. The program mainly consists of slow acceleration, followed by linearly increase and decrease. The slow acceleration period could initiate material flow, and the later stage is utilized to calculate dynamic yield stress and plastic viscosity, as the flow is more stable at this stage than during the period of acceleration. Dynamic yield stress indicates the stress required to maintain the flow. Therefore, a continuous up-down cycle is designed. The selected maximum shear rate of  $60 \text{ s}^{-1}$  is used to provided sufficient shear stress, while avoiding exorbitant stress beyond the tolerance of the machine. The selection of the testing program is based on those suggested in the literature [13,42]. As large amount of SF is employed, the rheology must be conducted without sand to limit extremely high viscosity.

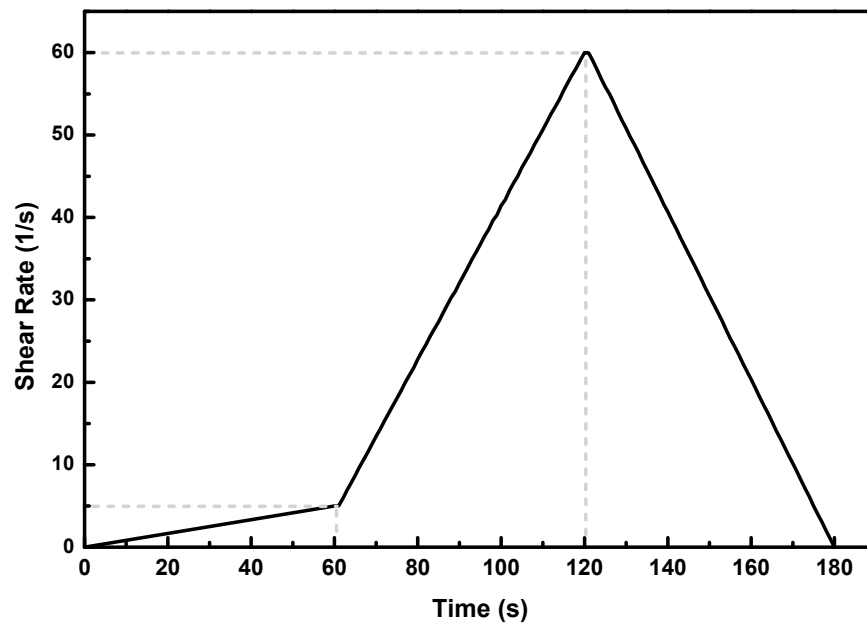


**Figure 4.** Program for rheology.

#### 2.3.4. Setting Time

The setting time of the mortar is evaluated using the methods in [43]. A digital tester, produced by Jinan Taiqin Electric Co. Ltd, was applied for penetration resistance. The initial setting is determined when a penetration resistance of 350 N is obtained with a 100 mm<sup>2</sup> (cross sectional area) nozzle. The final setting is determined when a penetration resistance of 560 N is achieved using a nozzle with a cross sectional area of 20 mm<sup>2</sup>.

#### 2.3.5. Drying Shrinkage

Drying shrinkage is tested based on the work of [44]. Three prisms with the size of 25 mm × 25 mm × 285 mm are cast for each mix, and a comparator is applied to measure the length change after the specimens are removed from the lime-saturated water, in accordance with standard. The specimens are immersed in lime-saturated water for 2 h before being moved into a chamber with humidity of 50% and a temperature of 25 °C.

#### 2.3.6. Surface pH

A pH100 pen-based ExStik<sup>®</sup> pH meter, produced by Extech Instruments from the USA, is employed to test the surface pH of the hardened matrix. The flat surface electrode is designed for easy on-the-spot pH measurements in liquids, semi-solids and solids.

#### 2.3.7. Compressive Strength

Compressive strength is tested, according to the methods used in [45]. The samples of 40 mm × 40 mm × 40 mm, at corresponding curing ages, are tested with a rate of 0.6 MPa/s for each batch.

#### 2.3.8. Printing Height

The printing height is measured with a 3D concrete printer (desktop type, NELD-3D736, Figure 5) produced by NELD Limited in Beijing. The moving speed of the gantry is 30 mm/s on the X/Y axis and 10 mm/s on the Z axis. The extruding speed of the extruder is 2.7 g/s, and the printing height for each layer is 7 mm. The path for verifying the printing height is a 20 mm × 200 mm × 230 mm rectangle. The diameter of the nozzle is 10 mm, and the printing height is instantly determined after the batch mixing.

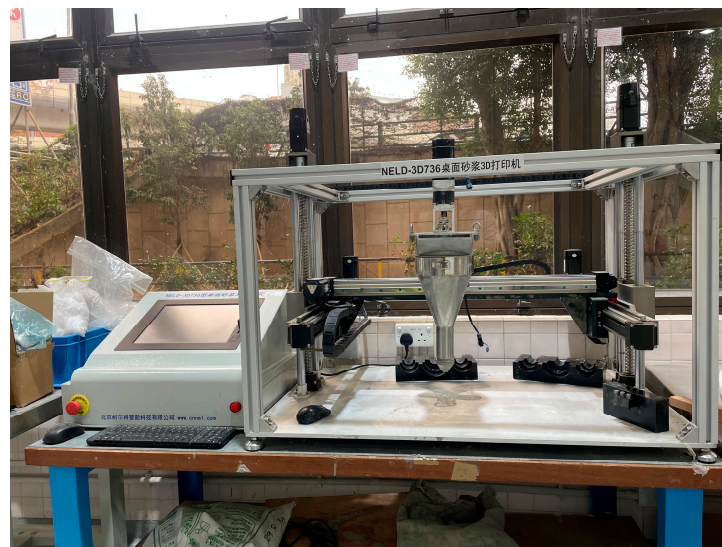


Figure 5. Desktop 3D concrete printer applied in this study.

### 3. Results and Discussion

#### 3.1. Slump Flow

Figure 6 demonstrates the slump flow of mixes in this study. The M-R group exhibits a slump spread of merely 135 mm, as SF possess an extremely small particle size (depicted in Table 1). It should be noted that the incorporation of additional SP fails to promote slump flow. The application of glass powder and slag increases the slump flow, which is attributed to smaller particle size. The combined employment of SF and slag decrease the potential of bleeding induced by SF. The partial replacement of OPC and SF with ISSA maintains the slump flow, which is induced by porous structure of ISSA [30–33]. The slump flow of A is adjusted to 185 mm, with a suitable ratio between water and dry materials.

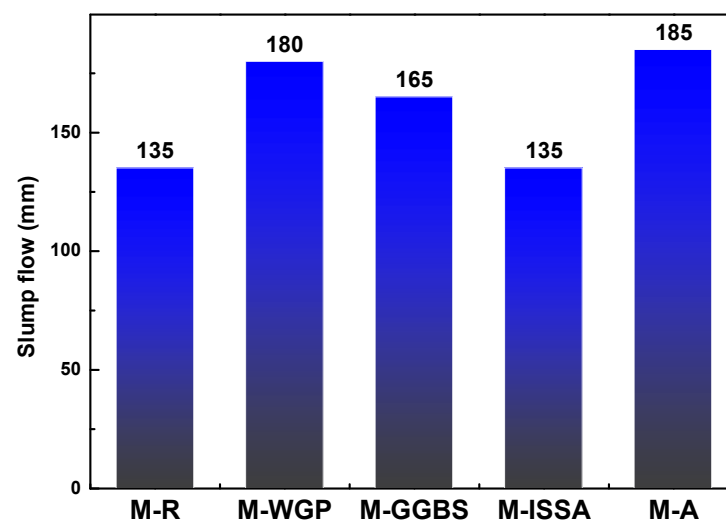


Figure 6. Slump flow of mixes in this study.

Generally, slump flow puts forward requirements towards extrudability and printability. Suitable slump flow is required to ensure that the mix can be extruded with good shape maintenance. In the literature, it is recommended that slump flow be set within 150–190 mm [39].

### 3.2. Buildability

Table 3 displays the results related to buildability test used in this study. It should be noted that the original height of the mortar before lifting the mold is 6.0 cm. The reduction rate of the height, before and after compression, is described using the buildability index. M-R exhibits the highest location, before and after compression, which is attributed to its lower workability, revealed in Figure 6. More importantly, M-R shows the lowest buildability index, indicating that it possesses the highest capability for shape maintenance.

**Table 3.** Results related to the buildability test used in this study.

ID	Height/cm		Buildability Index
	Before Compression	After Compression	
M-R	5.8	4.0	31%
M-WGP	4.3	2.7	37%
M-GGBS	5.2	2.3	56%
M-ISSA	5.2	3.3	37%
M-A	3.8	2.1	45%

However, the other three strategies all decrease the shape retention ability, to some degree. Therefore, we mainly discuss the height after compression and the buildability index, as the height before compression can be easily influenced by operators. The replacement of OPC and SF with WGP or GGBS decreases the remaining height, while application of ISSA maintains the ability to prevent deformation. This can be explained by the improved workability, which is totally in accordance with the higher slump spread shown in Figure 6. The application of ISSA maintains the ability to prevent deformation, to some degree, when comparing the printing height with M-WGP and M-GGBS. Correspondingly, decreased slump flow is observed in Figure 6. Thanks to its porous structures, ISSA contributes to a more inflexible slurry during printing. Moreover, Table 3 reveals that M-A exhibits the largest deficiency in regards to shape maintenance (height after compression), and it also consistently demonstrates the largest slump spread, as shown in Figure 6. In terms of the buildability index, nearly the same tendency is observed, with the exception of M-WGP. This is because the buildability index is also calculated from the height before compression. Therefore, it may be more suitable to evaluate the buildability using the height after compression.

Generally speaking, the slump test evaluates the workability of the slurry, and the result is closely related to the extrudability. The buildability index can satisfactorily complete the prediction regarding printing behaviors of 3D printing concrete, despite the fact that workability and buildability are correlated.

### 3.3. Rheology

Figure 7 presents the rheological curves of the pastes. Table 4 demonstrates the rheological parameters obtained from Figure 7. In Figure 7, dynamic yield stress and plastic viscosity are determined by linear fitting in the third stage. It is determined that the strategy of replacing OPC and SF with WGP decreases dynamic yield stress, but increases the plastic viscosity, to some degree. More importantly, less SF induces slower hydration and corresponding, lower thixotropy. The strategy of replacing OPC with GGBS results in lower yield stress and thixotropy. GGBS exhibits the capacity for rapid reaction, compared to other supplementary cementitious materials. The strategy of replacing OPC and SF with ISSA leads to milder reduction of yield stress and thixotropy. More importantly, the further decline in plastic viscosity is also observed.

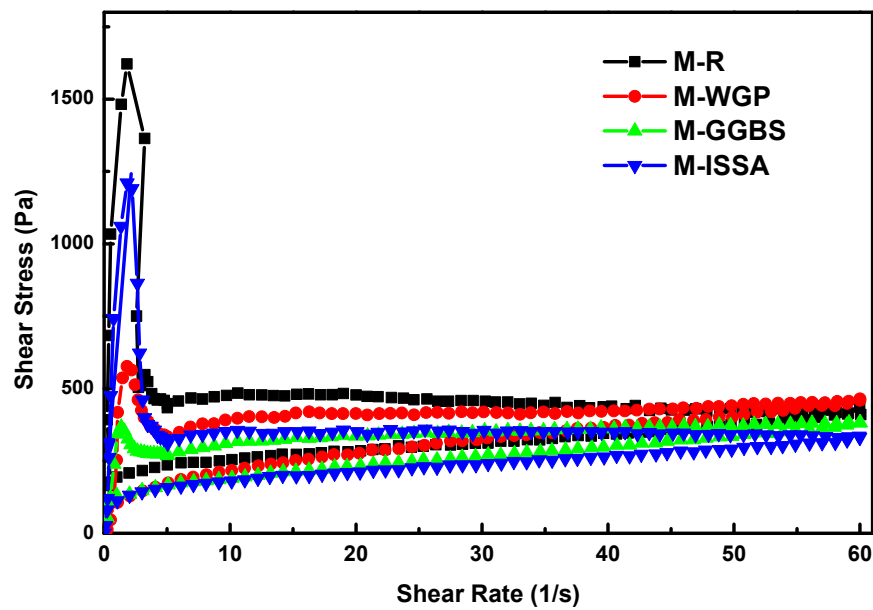


Figure 7. Rheological curves of the paste.

Table 4. Rheological parameters of the paste used in this study.

ID <sup>a</sup>	Dynamic Yield Stress/Pa	Plastic Viscosity/Pa·s	Thixotropy/Pa·s <sup>-1</sup>
M-R	219.3	3.2	6949.4
M-WGP	192.8	4.3	4922.4
M-GGBS	160.3	3.6	4082.9
M-ISSA	157.8	2.7	5567.4

<sup>a</sup> The paste phase of the commercial product could not be obtained; thus, it was not tested.

The yield stress and plastic viscosity should locate within a certain range. Suitable yield stress ensures correct extrudability and buildability. High-yield stress induces difficulties during extrusion, while low-yield stress leads to over spreading. Plastic viscosity also affects the printing behaviors to a remarkable extent. It is determined that the plastic viscosity of a printable mix most likely locates in the range of 1.6–5.8 Pa·s [46]. Sufficient viscosity guarantees the stability of the extruded filament, but excessive viscosity results in failure during extrusion.

It should be noted that higher thixotropy is not always a disadvantage. Faster setting-induced higher thixotropy can be applied to achieve higher printing height. Therefore, 3D printing technology holds specific requirements regarding yield stress, viscosity, and thixotropy.

### 3.4. Setting Time

Figure 8 presents the setting results for the M-GGBS and M-A groups. Compared with the M-GGBS group, M-A group exhibits much faster initial setting, which is attributed to its alkali activated system. The initial setting time for the M-GGBS and M-A groups are 201.0 min and 92.9 min, respectively. Faster setting ensures sufficient strength from the lower portion to support the upper layers during printing, from which even higher printing heights can be achieved.

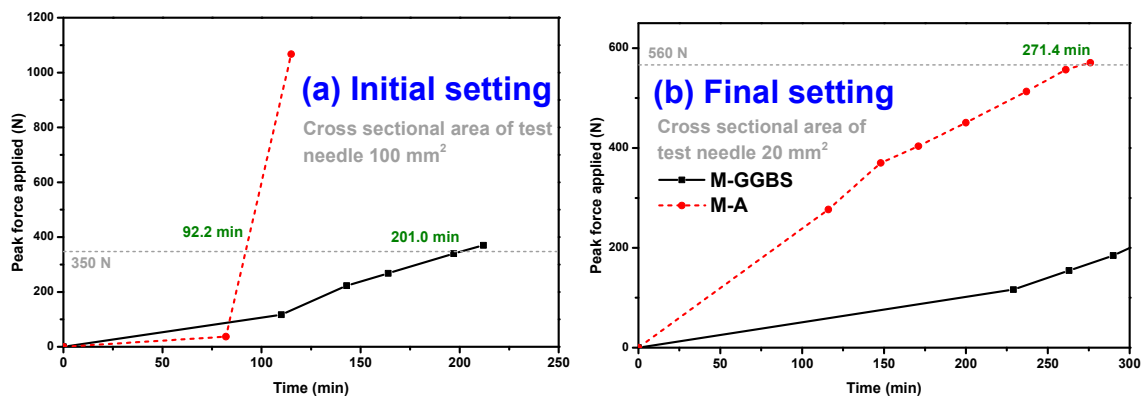


Figure 8. Setting results for the M-GGBS and M-A groups.

Figure 8 demonstrates the final setting results for the M-GGBS and M-A groups, which exhibit the same tendencies as Figure 6. The faster setting of the M-A group is attributed to the alkali activated binder inside.

### 3.5. Drying Shrinkage

Figure 9 depicts the drying shrinkage of the mixes in this study. Compared with the M-R group, the replacement of OPC and SF with WGP decreases drying shrinkage significantly. The results are in agreement with those in the literature [47]. This should be attributed to the OPC reduction and the slow dissolution rate of the glass powder. As is commonly known, drying shrinkage results from the loss of moisture from the hardened concrete surface to the environment and is controlled by capillary pressure within the concrete [48,49]. Firstly, small particles in the WGP fill the pores. Nevertheless, the dissolution of WGP in the pore solutions contributes to the refined pore structures [50]. The replacement of OPC with slag yields a limited effect on drying shrinkage, as slag possesses the capacity for rapid reaction and introduces significant chemical shrinkage [51]. The results are consistent with those in previous research [52]. ISSA incorporation induces a significant increase in drying shrinkage, from early to later age. This is related to the porous structure of ISSA, and subsequently, to water absorption, which is followed by more substantial evaporation [31]. The M-A group demonstrates the best volume stability, which should be attributed to the application of the expansive agent.

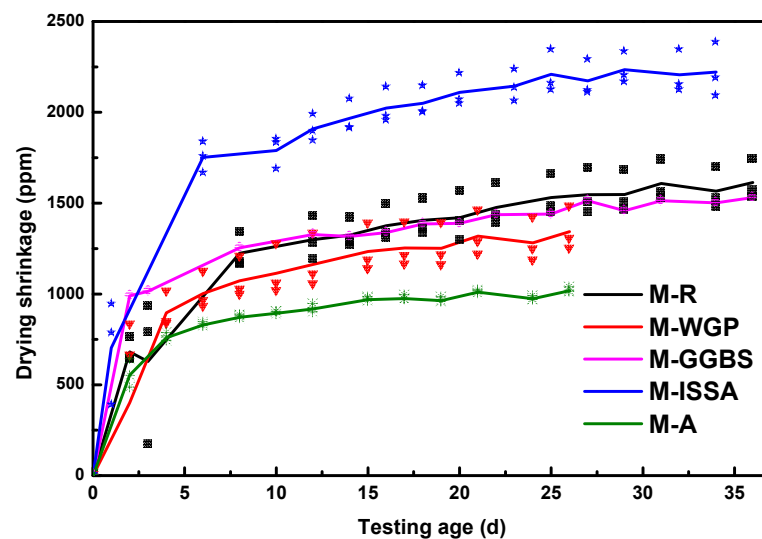


Figure 9. Drying shrinkage of mixes in this study.

More importantly, Figure 9 reveals that the development of the shrinkage rates in the early age are in the order of M-ISSA > M-GGBS > M-R > M-A > M-WGP. Generally, the shrinkage rate during an early age corresponds to the total shrinkage at later ages.

### 3.6. Surface pH

Figure 10 shows the surface pH of the mixes after 28 days of standard curing. Generally, the pH of the cement-based materials locates in the range of 12.5–13.5 [53–55]. It is revealed that the application of SF, and other materials, reduces the obtained pH, which is related to OPC diminution and the pozzolanic effect caused by the wastes. For a cement-based binding system, the pH is controlled by portlandite dissolution and alkali release. Employment of SF, and other wastes, decreases the portlandite generation and alkali release from OPC hydration.

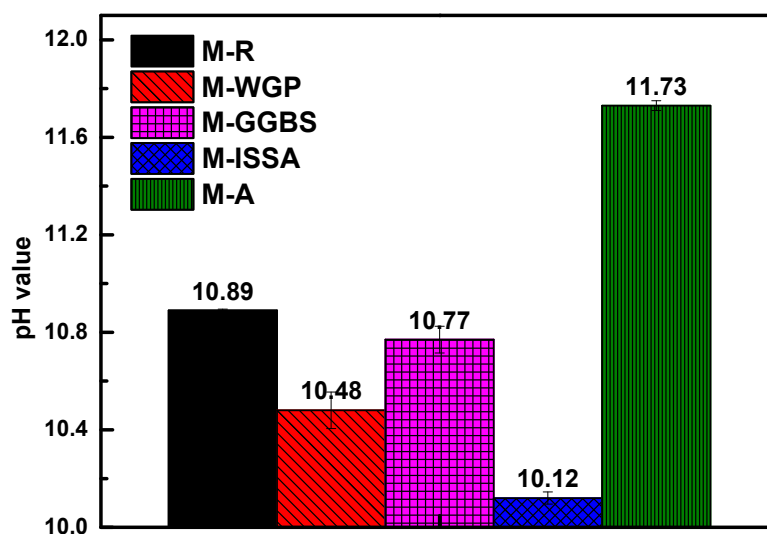


Figure 10. Surface pH of mixes after 28 days of curing.

Compared with the M-R group, the incorporation of WGP contributes to the lower pH attributed to the further decrease in the OPC content. Replacing OPC with SF maintains the pH, as the alkali consumption of slag is far lower than that of SF. As depicted in the literature, only a small to moderate reduction in portlandite is observed after the application of slag [56–58]. Moreover, slag even induces higher concentrations of alkali, under some circumstances [59]. The replacement of OPC and SF with ISSA exhibits the lowest pH, while commercially available A materials demonstrate the highest pH.

The solubility product constant of portlandite is  $5.5 \times 10^{-6}$ , inducing a corresponding pH of 12.2 [60], while the pH in the pore solution of the OPC used in this study is 12.8 after 28 days of standard curing, based on our previous research [61]. The increased pH indicates the alkali release capacity of OPC, while the much lower pH observed in the M-R, M-WGP, M-GGBS, M-ISSA, and M-A groups demonstrates the alkali consumption of the wastes.

The material is assumed to possess a constant capacity for alkali release or alkali consumption, as shown in Table 5, which is actually related to dosage. For easier operation, the alkalinity consumption of some wastes is also considered as alkalinity improvement.

Table 5. Alkalinity improvement capacity of the materials.

Material	OPC	SF	WGP	Slag	ISSA
Alkali release	a	b	c	d	e

Therefore, a set of equations can be deduced according to the data in Figure 10, as present in Equation (1).

$$\begin{cases} 100\% \times a = 10^{12.8-14} - 10^{12.2-14} \\ 60\% \times a + 40\% \times b = 10^{10.89-14} - 10^{12.2-14} \\ 40\% \times a + 20\% \times b + 40\% \times c = 10^{10.48-14} - 10^{12.2-14} \\ 20\% \times a + 40\% \times b + 40\% \times d = 10^{10.77-14} - 10^{12.2-14} \\ 50\% \times a + 30\% \times b + 20\% \times e = 10^{10.12-14} - 10^{12.2-14} \end{cases} \quad (1)$$

The results are presented in Equation (2). Based on the simplified calculation, OPC and slag are found to possess similar contributions to alkalinity, which is consistent with the results in the literature [56–58]. WGP and ISSA demonstrate a similar capacity for alkalinity consumption, which is mainly attributed to their limited activity during cement hydration. SF exhibits the best capacity for alkalinity consumption, which is the reason why SF is essential for low-pH concrete.

$$\begin{cases} a = 0.048 \\ b = -0.109 \\ c = -0.032 \\ d = 0.047 \\ e = -0.034 \end{cases} \quad (2)$$

### 3.7. Compressive Strength

Figure 11 presents the compressive strength of the mixes after standard and steam curing.

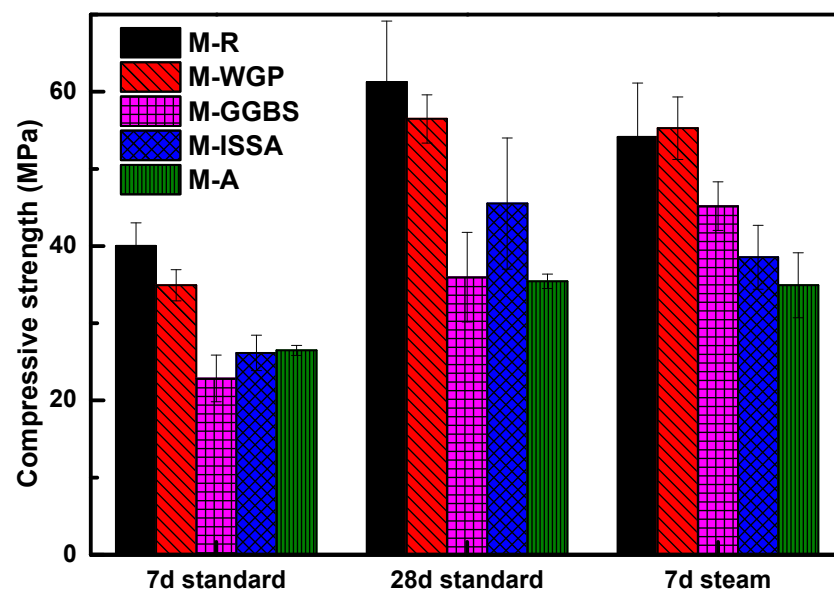


Figure 11. Compressive strength of the mixes in this study.

Under standard curing, the compressive strength of M-R reaches 40 MPa and 60 MPa after 7 days and 28 days, respectively. However, waste replacement exerts a significant influence on strength development. The M-WGP group shows comparable strength to the M-R group, as the M-WGP group is equipped with improved workability, allowing for better compaction. As presented in Figure 11, the strength of M-WGP reaches 35.0 MPa and 56.5 MPa after 7 days and 28 days, respectively. Based on the literature, the dissolution rate of glass powder reaches around 40% at a 10% dosage and 25% at a 20% dosage [62]. Therefore, WGP should partially contribute to strength, with a pozzolanic effect. The M-GGBS group demonstrates lower strength. Specifically, the compression strength at 7 day and 28 day is 28.8 MPa and 36.0 MPa, respectively. The decreased strength should

be attributed to the lowest cement dosage, as presented in Table 2. GGBS is frequently regarded as the closest supplementary cementitious materials to cement, and it should exhibit strength comparable to M-R. However, owing to the fact that its activation on GGBS requires a certain amount of portlandite, the system without sufficient portlandite (such as M-GGBS) cannot fully activate the GGBS, leading to a notable decline in strength.

The M-ISSA group shows higher strength because of its sufficient cement dosage. After 7 day and 28 of standard curing, the compressive strength reaches 26.2 MPa and 45.5 MPa, respectively. It should be noted that additives can also influence mechanical properties. It is revealed that the SP hinders the early hydration of cement and induces lower cement hydration, but the retardation decreases with further cement hydration [63,64]. HPMC decreases the defoaming effect of vibration, inducing lower strength [65].

Steam curing leads to comparable strength after 28 days of standard curing. It seems that high temperatures promote the strength of the group with WGP, which is also in agreement with the results in the literature [66]. This is related to the higher dissolution rate of glass powder under higher temperatures.

### 3.8. Printing Height

Figure 12 displays the printing height of the mixes used in this study. Generally, printability is applied to describe the capacity of the mixture to be printed. In fact, printability includes extrudability and buildability, which depicts the ability to be extruded and to maintain its shape after extrusion, respectively. The M-R group exhibits a printing height of 130 mm after batch mixing. The relatively lower height is related to excessive yield strength induced by the high OPC and SF content, as revealed in Table 4. This is supported by the lower slump flow reate, despite the high dosage of SP, as presented in Figure 6. Excessive yield strength means that the mixture cannot be smoothly extruded. However, the strategy of replacing OPC and SF with WGP (M-WGP group) decreases the yield strength of the mixture, which contributes to higher slump flow and fewer difficulties during extrusion. Unfortunately, this strategy leads to a lower capacity for shape maintenance, causing its early collapse during printing.

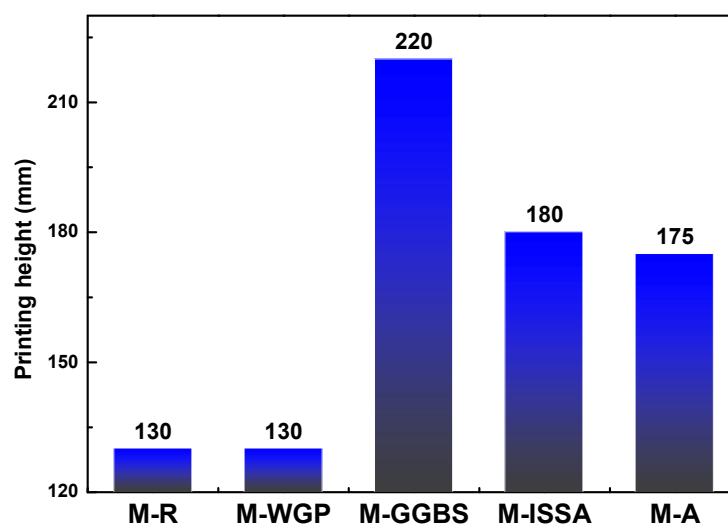
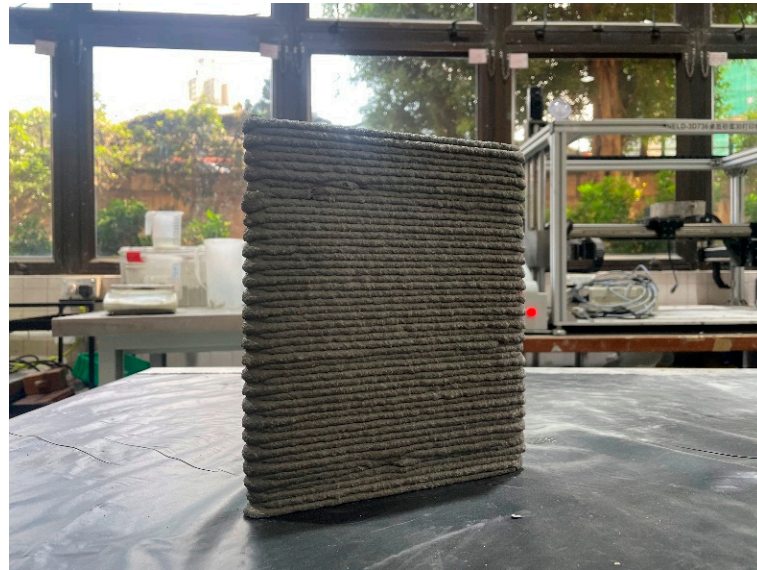


Figure 12. Printing height of the mixes used in this study.

The strategy of replacing OPC with slag (M-GGBS group, Figure 13) improves the workability and corresponding extrudability, while consistent SF ensures the viscosity needed for printing and exhibits the best buildability. As presented in Table 4, this strategy slightly increases plastic viscosity when compared with that of M-R. Therefore, the printability of the M-GGBS group is significantly improved.



**Figure 13.** Product obtained from the printing height test of the M-GGBS group.

Limited replacement of OPC and SF with ISSA (M-ISSA group) contributes to a reasonable printing height, as the buildability is significantly promoted. This can be attributed to reduced yield stress, leading to fewer difficulties during extrusion, as presented in Table 4. Compared with material A, the ternary systems of OPC-SF-slag and OPC-SF-ISSA exhibit even better printing performance.

Figure 14 demonstrates the relationship between slump flow and printing height after batch mixing. There is no obvious correlation between slump flow and printing height. This indicates that slump flow holds certain information regarding 3D printing, but also lacks other facts. Therefore, it is not recommended to propose slump flow as the indicator for predicting printing behaviors.

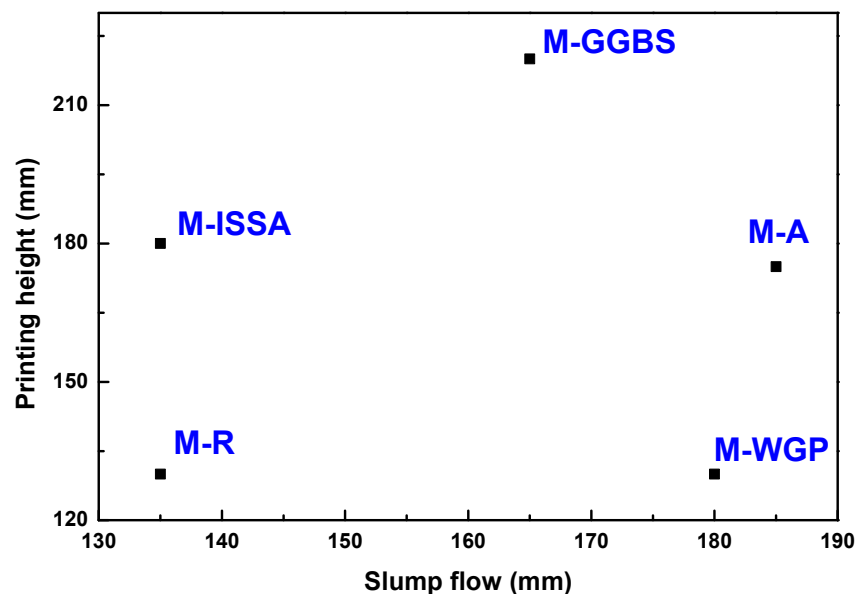


**Figure 14.** Relationship between slump flow and printing height after batch mixing.

### 3.9. Visual Observation

Figure 15 presents the appearance observed when the M-GGBS and M-A groups are applied to printing the samples. The M-GGBS group exhibits much better surface area com-

pared with that of the commercially available A group. This is related to the employment of high-dosage SF, inducing much higher viscosity and consistency during printing.



Figure 15. Appearance observed: (a) M-GGBS group, (b) M-A group.

#### 4. Conclusions

In this study, several solid wastes available in Hong Kong are applied to develop 3D printing concrete with low carbon and low pH. Comprehensive investigations on fresh behaviors, volume stability, surface pH, and mechanical properties are conducted. The following conclusions can be drawn:

- (1) Better printability is achieved by replacing OPC and SF in the classic low-pH recipe with slag and ISSA, which contributes to lower yield stress and reduced shape maintenance. Excessive yield stress induced by high-dosage SF in a low pH recipe can be controlled by the reasonable application of solid wastes, herein improving the extrudability and buildability. No obvious correlation between slump flow and printing height is observed.
- (2) Lower surface pH is actualized with the partial replacement of OPC and SF with WGP, slag, and ISSA, which consequently results in lower compressive strength. The outstanding pH control in SF is revealed after approximate quantification of the contribution of all binders on the surface pH. Reducing OPC and increasing SF content is determined to be the most effective approach for low-pH concrete development.

**Author Contributions:** Conceptualization, X.-S.L., L.L. and S.Z.; Methodology, X.-S.L.; Software, L.L.; Formal analysis, X.-S.L.; Investigation, X.-S.L.; Writing—original draft, X.-S.L.; Writing—review & editing, L.L. and S.Z.; Supervision, L.L. All authors have read and agreed to the published version of the manuscript.

**Funding:** This research received no external funding.

**Data Availability Statement:** Data available on reasonable request from the authors. The data are not publicly available due to privacy restrictions.

**Conflicts of Interest:** The authors declare no conflict of interest.

#### References

1. Bach, T.; Coumes, C.C.D.; Pochard, I.; Mercier, C.; Revel, B.; Nonat, A. Influence of temperature on the hydration products of low pH cements. *Cem. Concr. Res.* **2012**, *42*, 805–817. [[CrossRef](#)]
2. Vogt, C.; Lagerblad, B.; Wallin, K.; Baldy, F.; Jonasson, J.-E. *Low pH Self Compacting Concrete for Deposition Tunnel Plugs*; Swedish Nuclear Fuel and Waste Management, Co.: Stockholm, Sweden, 2009.
3. Dauzères, A.; Le Bescop, P.; Cau-Dit-Coumes, C.; Brunet, F.; Bourbon, X.; Timonen, J.; Voutilainen, M.; Chomat, L.; Sardini, P. On the physico-chemical evolution of low-pH and CEM I cement pastes interacting with Callovo-Oxfordian pore water under its in situ CO<sub>2</sub> partial pressure. *Cem. Concr. Res.* **2014**, *58*, 76–88. [[CrossRef](#)]
4. Nochaiya, T.; Wongkeo, W.; Chaipanich, A. Utilization of fly ash with silica fume and properties of Portland cement–fly ash–silica fume concrete. *Fuel* **2010**, *89*, 768–774. [[CrossRef](#)]

5. Mazloom, M.; Ramezani-pour, A.A.; Brooks, J.J. Effect of silica fume on mechanical properties of high-strength concrete. *Cem. Concr. Compos.* **2004**, *26*, 347–357. [\[CrossRef\]](#)
6. Siddique, R. Utilization of silica fume in concrete: Review of hardened properties. *Resour. Conserv. Recycl.* **2011**, *55*, 923–932. [\[CrossRef\]](#)
7. Ahmed, A.S.; Elshikh, M.M.Y.; Elemam, W.E.; Youssf, O. Influence of Mixing-Water Magnetization Method on the Performance of Silica Fume Concrete. *Buildings* **2023**, *13*, 44. [\[CrossRef\]](#)
8. Wang, B.; Zhai, M.; Yao, X.; Wu, Q.; Yang, M.; Wang, X.; Huang, J.; Zhao, H. Printable and Mechanical Performance of 3D Printed Concrete Employing Multiple Industrial Wastes. *Buildings* **2022**, *12*, 374. [\[CrossRef\]](#)
9. Calvo, J.G.; Hidalgo, A.; Alonso, C.; Luco, L.F. Development of low-pH cementitious materials for HLRW repositories: Resistance against ground waters aggression. *Cem. Concr. Res.* **2010**, *40*, 1290–1297. [\[CrossRef\]](#)
10. Cheng, A.; Lin, W.-T.; Chao, S.-J.; Hsu, H.-M. Composition and selected properties of low pH mortars and concretes for radioactive waste repositories. *MATEC Web Conf.* **2020**, *322*, 01033. [\[CrossRef\]](#)
11. Buswell, R.A.; Leal de Silva, W.R.; Jones, S.Z.; Dirrenberger, J. 3D printing using concrete extrusion: A roadmap for research. *Cem. Concr. Res.* **2018**, *112*, 37–49. [\[CrossRef\]](#)
12. Zhang, C.; Deng, Z.; Zhang, Y.; Chen, C. Predicting the yield stress of 3d printing mortar based on the flowability of paste and excess paste thickness. In Proceedings of the 4th International Rilem Conference on Microstructure Related Durability of Cementitious Composites, The Hague, The Netherlands, 29 April 2021.
13. Zou, S.; Xiao, J.; Duan, Z.; Ding, T.; Hou, S. On rheology of mortar with recycled fine aggregate for 3D printing. *Constr. Build. Mater.* **2021**, *311*, 125312. [\[CrossRef\]](#)
14. Xiao, J.; Zou, S.; Yu, Y.; Wang, Y.; Ding, T.; Zhu, Y.; Yu, J.; Li, S.; Duan, Z.; Wu, Y.; et al. 3D recycled mortar printing: System development, process design, material properties and on-site printing. *J. Build. Eng.* **2020**, *32*, 101779. [\[CrossRef\]](#)
15. Moelich, G.M.; Kruger, P.J.; Combrinck, R. A plastic shrinkage cracking risk model for 3D printed concrete exposed to different environments. *Cem. Concr. Compos.* **2022**, *130*, 104516. [\[CrossRef\]](#)
16. Moelich, G.M.; Kruger, P.J.; Combrinck, R. The effect of restrained early age shrinkage on the interlayer bond and durability of 3D printed concrete. *J. Build. Eng.* **2021**, *43*, 102857. [\[CrossRef\]](#)
17. Moelich, G.M.; Kruger, P.J.; Combrinck, R. Mitigating early age cracking in 3D printed concrete using fibres, superabsorbent polymers, shrinkage reducing admixtures, B-CSA cement and curing measures. *Cem. Concr. Res.* **2022**, *159*, 106862. [\[CrossRef\]](#)
18. Daher, J.; Kleib, J.; Benzerzour, M.; Abriak, N.-E.; Aouad, G. Recycling of Flash-Calcined Dredged Sediment for Concrete 3D Printing. *Buildings* **2022**, *12*, 1400. [\[CrossRef\]](#)
19. Melichar, J.; Žižková, N.; Brožovský, J.; Mészárosová, L.; Hermann, R. Study of the Interaction of Cement-Based Materials for 3D Printing with Fly Ash and Superabsorbent Polymers. *Buildings* **2022**, *12*, 2008. [\[CrossRef\]](#)
20. Muthukrishnan, S.; Kua, H.W.; Yu, L.N.; Chung, J.K.H. Fresh Properties of Cementitious Materials Containing Rice Husk Ash for Construction 3D Printing. *J. Mater. Civ. Eng.* **2020**, *32*, 04020195. [\[CrossRef\]](#)
21. Ma, G.; Li, Z.; Wang, L. Printable properties of cementitious material containing copper tailings for extrusion based 3D printing. *Constr. Build. Mater.* **2018**, *162*, 613–627. [\[CrossRef\]](#)
22. Vaitkevičius, V.; Šerelis, E.; Hilbig, H. The effect of glass powder on the microstructure of ultra high performance concrete. *Constr. Build. Mater.* **2014**, *68*, 102–109. [\[CrossRef\]](#)
23. Mirzahosseini, M.; Riding, K.A. Influence of different particle sizes on reactivity of finely ground glass as supplementary cementitious material (SCM). *Cem. Concr. Compos.* **2015**, *56*, 95–105. [\[CrossRef\]](#)
24. Elaqla, H.; Rustom, R. Effect of using glass powder as cement replacement on rheological and mechanical properties of cement paste. *Constr. Build. Mater.* **2018**, *179*, 326–335. [\[CrossRef\]](#)
25. Mejdji, M.; Wilson, W.; Saillio, M.; Chaussadent, T.; Divet, L.; Tagnit-Hamou, A. Quantifying glass powder reaction in blended-cement pastes with the Rietveld-PONKCS method. *Cem. Concr. Res.* **2020**, *130*, 105999. [\[CrossRef\]](#)
26. Ting, G.H.A.; Tay, Y.W.D.; Qian, Y.; Tan, M.J. Utilization of recycled glass for 3D concrete printing: Rheological and mechanical properties. *J. Mater. Cycles Waste Manag.* **2019**, *21*, 994–1003. [\[CrossRef\]](#)
27. Cuevas, K.; Chougan, M.; Martin, F.; Ghaffar, S.H.; Stephan, D.; Sikora, P. 3D printable lightweight cementitious composites with incorporated waste glass aggregates and expanded microspheres—Rheological, thermal and mechanical properties. *J. Build. Eng.* **2021**, *44*, 102718. [\[CrossRef\]](#)
28. Liu, J.; Li, S.; Gunasekara, C.; Fox, K.; Tran, P. 3D-printed concrete with recycled glass: Effect of glass gradation on flexural strength and microstructure. *Constr. Build. Mater.* **2022**, *314*, 125561. [\[CrossRef\]](#)
29. Ting, G.H.A.; Tay, Y.W.D.; Tan, M.J. Experimental measurement on the effects of recycled glass cullets as aggregates for construction 3D printing. *J. Clean. Prod.* **2021**, *300*, 126919. [\[CrossRef\]](#)
30. Lu, J.-X.; Zhou, Y.; He, P.; Wang, S.; Shen, P.; Poon, C.S. Sustainable reuse of waste glass and incinerated sewage sludge ash in insulating building products: Functional and durability assessment. *J. Clean. Prod.* **2019**, *236*, 117635. [\[CrossRef\]](#)
31. Chen, Z.; Poon, C.S. Comparative studies on the effects of sewage sludge ash and fly ash on cement hydration and properties of cement mortars. *Constr. Build. Mater.* **2017**, *154*, 791–803. [\[CrossRef\]](#)
32. Chen, Z.; Li, J.S.; Poon, C.S. Combined use of sewage sludge ash and recycled glass cullet for the production of concrete blocks. *J. Clean. Prod.* **2018**, *171*, 1447–1459. [\[CrossRef\]](#)

33. Li, J.-S.; Guo, M.-Z.; Xue, Q.; Poon, C.S. Recycling of incinerated sewage sludge ash and cathode ray tube funnel glass in cement mortars. *J. Clean. Prod.* **2017**, *152*, 142–149. [\[CrossRef\]](#)
34. Ki, D.; Kang, S.Y.; Park, K.-M. Upcycling of Wastewater Sludge Incineration Ash as a 3D Printing Technology Resource. *Front. Sustain.* **2021**, *2*, 1–9. [\[CrossRef\]](#)
35. Zou, S.; Xiao, J.; Ding, T.; Duan, Z.; Zhang, Q. Printability and advantages of 3D printing mortar with 100% recycled sand. *Constr. Build. Mater.* **2021**, *273*, 121699. [\[CrossRef\]](#)
36. Ding, T.; Xiao, J.; Zou, S.; Wang, Y. Hardened properties of layered 3D printed concrete with recycled sand. *Cem. Concr. Compos.* **2020**, *113*, 103724. [\[CrossRef\]](#)
37. Ding, T.; Xiao, J.; Zou, S.; Zhou, X. Anisotropic behavior in bending of 3D printed concrete reinforced with fibers. *Compos. Struct.* **2020**, *254*, 112808. [\[CrossRef\]](#)
38. Kim, J.-S.; Kwon, S.-K.; Sanchez, M.; Cho, G.-C. Geological storage of high level nuclear waste. *KSCE J. Civ. Eng.* **2011**, *15*, 721–737. [\[CrossRef\]](#)
39. Tay, Y.W.D.; Qian, Y.; Tan, M.J. Printability region for 3D concrete printing using slump and slump flow test. *Compos. Part B Eng.* **2019**, *174*, 106968. [\[CrossRef\]](#)
40. *EN 1015-3:1999*; Methods of test for mortar for masonry-Part 3: Determination of consistence of fresh mortar (by flow table). iTeh, Inc.: Newark, DE, USA, 1999.
41. Arunothayan, A.R.; Nematollahi, B.; Ranade, R.; Bong, S.H.; Sanjayan, J. Development of 3D-printable ultra-high performance fiber-reinforced concrete for digital construction. *Constr. Build. Mater.* **2020**, *257*, 119546. [\[CrossRef\]](#)
42. Weng, Y.; Li, M.; Tan, M.J.; Qian, S. Design 3D printing cementitious materials via Fuller Thompson theory and Marston-Percy model. *Constr. Build. Mater.* **2018**, *163*, 600–610. [\[CrossRef\]](#)
43. *ASTM C403/403M-08*; Standard Test Method for Time of Setting of Concrete Mixtures by Penetration Resistance. ASTM International: West Conshohocken, PA, USA, 2008; p. 7.
44. *ASTM C157/C157M-08*; Standard Test Method for Length Change of Hardened Hydraulic-Cement Mortar and Concrete. ASTM International: West Conshohocken, PA, USA, 2014.
45. *BS EN 1015-11:2019*; Methods of Test for Mortar for Masonry—Part 11: Determination of Flexural and Compressive Strength of Hardened Mortar. iTeh, Inc.: Newark, DE, USA, 1999.
46. Rehman, A.U.; Kim, J.-H. 3D Concrete Printing: A Systematic Review of Rheology, Mix Designs, Mechanical, Microstructural, and Durability Characteristics. *Materials* **2021**, *14*, 3800. [\[CrossRef\]](#)
47. Chen, X.; Chen, H.; Tan, W. Effect of glass powder on the mechanical and drying shrinkage of glass-fiber-reinforced cementitious composites. *Case Stud. Constr. Mater.* **2022**, *17*, e01587. [\[CrossRef\]](#)
48. Huang, D.; Chen, P.; Peng, H.; Yang, Y.; Yuan, Q.; Su, M. A review and comparison study on drying shrinkage prediction between alkali-activated fly ash/slag and ordinary Portland cement. *Constr. Build. Mater.* **2021**, *305*, 124760. [\[CrossRef\]](#)
49. Di Bella, C. *Drying Shrinkage of Cementitious Materials at Early Age*; ETH Zurich: Zurich, Switzerland, 2016.
50. Nahi, S.; Leklou, N.; Khelidj, A.; Oudjit, M.N.; Zenati, A. Properties of cement pastes and mortars containing recycled green glass powder. *Constr. Build. Mater.* **2020**, *262*, 120875. [\[CrossRef\]](#)
51. Lothenbach, B.; Le Saout, G.; Haha, M.B.; Figi, R.; Wieland, E. Hydration of a low-alkali CEM III/B-SiO<sub>2</sub> cement (LAC). *Cem. Concr. Res.* **2012**, *42*, 410–423. [\[CrossRef\]](#)
52. Zhu, Y.; Yang, Y.; Yao, Y. Use of slag to improve mechanical properties of engineered cementitious composites (ECCs) with high volumes of fly ash. *Constr. Build. Mater.* **2012**, *36*, 1076–1081. [\[CrossRef\]](#)
53. Duffó, G.S.; Morris, W.; Raspini, I.; Saragovi, C. A study of steel rebars embedded in concrete during 65 years. *Corros. Sci.* **2004**, *46*, 2143–2157. [\[CrossRef\]](#)
54. Maruthapandian, V.; Saraswathy, V.; Muralidharan, S. Development of solid state embeddable reference electrode for corrosion monitoring of steel in reinforced concrete structures. *Cem. Concr. Compos.* **2016**, *74*, 100–108. [\[CrossRef\]](#)
55. Montemor, M.F.; Simões, A.M.P.; Salta, M.M. Effect of fly ash on concrete reinforcement corrosion studied by EIS. *Cem. Concr. Compos.* **2000**, *22*, 175–185. [\[CrossRef\]](#)
56. Kocaba, V. *Development and Evaluation of Methods to Follow Microstructural Development of Cementitious Systems Including Slags*; EPFL: Lausanne, Switzerland, 2009.
57. Pane, I.; Hansen, W. Investigation of blended cement hydration by isothermal calorimetry and thermal analysis. *Cem. Concr. Res.* **2005**, *35*, 1155–1164. [\[CrossRef\]](#)
58. Escalante, J.I.; Gómez, L.Y.; Johal, K.K.; Mendoza, G.; Mancha, H.; Méndez, J. Reactivity of blast-furnace slag in Portland cement blends hydrated under different conditions. *Cem. Concr. Res.* **2001**, *31*, 1403–1409. [\[CrossRef\]](#)
59. Luke, K.; Lachowski, E. Internal Composition of 20-Year-Old Fly Ash and Slag-Blended Ordinary Portland Cement Pastes. *J. Am. Ceram. Soc.* **2008**, *91*, 4084–4092. [\[CrossRef\]](#)
60. Schmuckler, J.S. Solubility product constant,  $K_{sp}$ . *J. Chem. Educ.* **1982**, *59*, 245. [\[CrossRef\]](#)
61. Hu, X.; Poon, C.S. Chloride-related steel corrosion initiation in cement paste prepared with the incorporation of blast-furnace slag. *Cem. Concr. Compos.* **2022**, *126*, 104349. [\[CrossRef\]](#)
62. Mejdí, M.; Wilson, W.; Saillio, M.; Chaussadent, T.; Divet, L.; Tagnit-Hamou, A. Hydration and microstructure of glass powder cement pastes—A multi-technique investigation. *Cem. Concr. Res.* **2022**, *151*, 106610. [\[CrossRef\]](#)
63. Alsadey, S.J. Effect of superplasticizer on fresh and hardened properties of concrete. *Engineering* **2015**, *1*, 70–74.

64. Kong, F.-r.; Pan, L.-s.; Wang, C.-m.; Zhang, D.-l.; Xu, N. Effects of polycarboxylate superplasticizers with different molecular structure on the hydration behavior of cement paste. *Constr. Build. Mater.* **2016**, *105*, 545–553. [[CrossRef](#)]
65. Gu, X.; Li, X.; Zhang, W.; Gao, Y.; Kong, Y.; Liu, J.; Zhang, X. Effects of HPMC on Workability and Mechanical Properties of Concrete Using Iron Tailings as Aggregates. *Materials* **2021**, *14*, 6451. [[CrossRef](#)] [[PubMed](#)]
66. Kou, S.C.; Xing, F. The Effect of Recycled Glass Powder and Reject Fly Ash on the Mechanical Properties of Fibre-Reinforced Ultrahigh Performance Concrete. *Adv. Mater. Sci. Eng.* **2012**, *2012*, 263243. [[CrossRef](#)]

**Disclaimer/Publisher's Note:** The statements, opinions and data contained in all publications are solely those of the individual author(s) and contributor(s) and not of MDPI and/or the editor(s). MDPI and/or the editor(s) disclaim responsibility for any injury to people or property resulting from any ideas, methods, instructions or products referred to in the content.